

Evolution of an Arched Magnetized Laboratory Plasma in a Sheared Magnetic Field

Kamil D. Sklodowski¹†, Shreekrishna Tripathi¹ and Troy Carter¹

¹Physics and Astronomy, University of California, Los Angeles, CA 90095, USA

(Received xx; revised xx; accepted xx)

Arched magnetized structures are a common occurrence in space and laboratory plasma. Results from a laboratory experiment on spatio-temporal evolution of an arched magnetized plasma ($\beta \approx 10^{-3}$, Lundquist number $\approx 10^4$, plasma radius/ion gyroradius ≈ 20) in a sheared magnetic configuration have been discussed. The experiment is designed to model conditions relevant to formation and destabilization of similar structures in the solar atmosphere. The direction of a nearly horizontal overlying magnetic field was varied to study two different regimes of magnetic forces that assist or inhibit expansion of the arched plasma. The electrical current in the arched plasma was well below the current required to make it kink unstable. A significant increase in the writhe of the arched plasma and formation of a magnetized plasma jet were key observations when overlying magnetic field was oriented to inhibit its expansion.

1. Introduction

Arched magnetized plasma structures are abundant across all layers of the solar atmosphere. Solar prominences and coronal loops are notable examples of such structures that confine a current carrying plasma by closed magnetic fields. Magnetic loops in solar corona have characteristically low plasma beta ($\beta \approx 10^{-3} - 10^{-2}$) which means these loops are nearly force free (Török *et al.* 2004; Wiegelmann & Sakurai 2012). Typical length of these structures is on the order of $10^7 - 10^8$ m (Chen 2017). A photograph of a solar prominence, its simplified schematic, and laboratory arrangement to model the prominence eruption have been depicted in figure 1.

Solar prominences usually remain confined from days to few weeks (Lang 2001; Chen 1996; Hildner *et al.* 1975; Cremades & Bothmer 2004). Sporadically some of these structures loose confinement and erupt due to loss of equilibrium (Abbot 1911; Rosner *et al.* 1978; Burlaga 1988; Rust 1994). The relatively stable pre-eruption phase for these structures lasts for several thousands Alfvén transit times (time taken by the Alfvén wave to travel from one to other footpoint of the arched plasma). Solar eruptive events (e.g. coronal mass ejections (CME), solar jets, and solar flares) are among the most energetic events associated with the eruption of plasmas in the solar system. It is estimated that each eruption releases $10^{30} - 10^{33}$ ergs of energy in the form of kinetic energy of the bulk plasma motion and electromagnetic radiation (Chen 2017). In this process, a large amount of mass ($10^{14} - 10^{16}$ g) are expelled at high velocities, which upon reaching Earth, can cause undesirable effects. These effects include geomagnetic storms, damages to power transmission lines and communication satellites systems, as well as threat to astronauts in space (Thomson *et al.* 2010). Exploration of physical mechanism driving solar eruptions continues to be an open area of research. A rather well known candidate for eruption trigger is a kink instability, proposed after observations of helical deformations (writhe and twist) of erupting solar prominences (Fan 2005; Török & Kliem 2005; Sturrock *et al.* 2001; Sakurai 1976).

Improved understanding of processes that lead to eruptions and affect the dynamics of arched

† Email address for correspondence: ksklodowski@ucla.edu

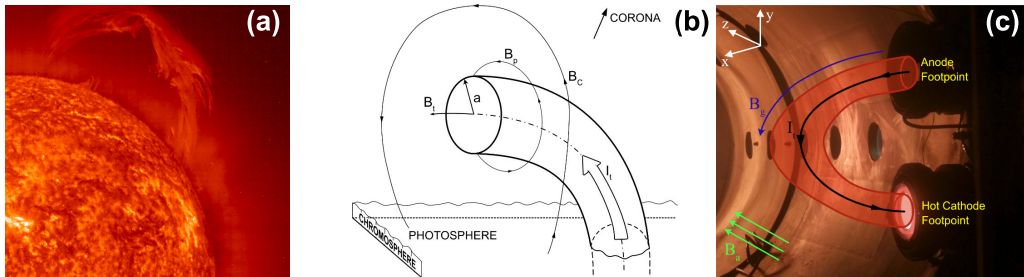


Figure 1: (a) A solar prominence observed in extreme ultraviolet (EUV) wavelength of 304 by the SOHO spacecraft on 28 March 2000 (Credit: NASA). (b) Schematic of a model flux rope in solar corona with overlying strapping field B_c . Minor radius a and flux rope current I_t are indicated. Toroidal and poloidal components of magnetic field are B_t and B_p , respectively. Adapted from (Chen 2017). (c) Photograph of the experimental setup depicting a current filament I_t , guiding magnetic field B_g and ambient magnetic field B_a .

magnetized plasmas is of utmost importance for prediction of solar energetic events. A laboratory plasma experiment was designed at UCLA to address this important area (Tripathi & Gekelman 2010). The experiment facilitates *in situ* measurements on varieties of arched current-carrying magnetized plasma (figure 1c). The foot-points of the arched plasma are anchored on cathode and anode which impose line-tied boundary conditions at both ends of the arch. Plasma parameters in the experiment are appropriately scaled to capture the essential physics of arched plasma on the Sun (Tripathi & Gekelman 2010). Development of writhe and/or twist of the arched plasma in the presence of a strong overlying magnetic field is the main focus of this paper.

Modeling solar prominences in laboratory or simulation often involves creation of flux ropes - twisted magnetic structures due to significant poloidal magnetic field generated by the toroidal electrical current (see figure 1 for flux-rope co-ordinates) (Török *et al.* 2011; Fan 2005; Low 2001; Chen 2011). A kink-unstable magnetic flux rope with electrical current along externally imposed toroidal magnetic field, B_t , is expected to develop writhe due to dominance of self-generated magnetic field, B_p . Quantitatively, writhe is a measure of net self-coiling of magnetic-field lines and is related to its total torsion (Török *et al.* 2014). Writhe is dependent on the magnitude of electrical current and toroidal magnetic field. Therefore, it is also related to magnetic helicity through $H = F^2(T + W)$; where H is the relative helicity, F is the axial magnetic flux, W is the writhe, and T is the number of turns of the field line (Berger & Prior 2006). Same formula applies to flux ropes with line-tied boundary conditions at both foot-points. Under ideal MHD assumptions (justified for solar prominences and their simulations), the magnetic helicity is nearly conserved. Therefore, the twist and writhe are closely coupled to each other. The total twist, Φ , can be expressed as (Hood & Priest 1981),

$$\Phi = \frac{lB_\phi(r)}{rB_z(r)}, \quad (1.1)$$

where l is the length of the flux rope, r is the minor radius, B_z is the axial magnetic field, and B_ϕ is the azimuthal magnetic field. When the twist exceeds a critical value Φ_c , the system becomes kink unstable and evolves to reduce the curvature of magnetic field lines. This process lowers the net magnetic energy of the system and effectively converts the twist into writhe (Shafranov 1957; Kruskal & Tuck 1958; Freidberg 1982; Priest 1982). For line-tied magnetic arches (aspect ratio = major radius/minor radius ≈ 5), the critical value of the twist parameter, Φ_c , was estimated to be $\approx 3.5\pi$ (Török *et al.* 2004). Although the exact nature of the stored magnetic energy prior to solar eruptions is still a matter of debate, the free magnetic energy stored in sheared magnetic

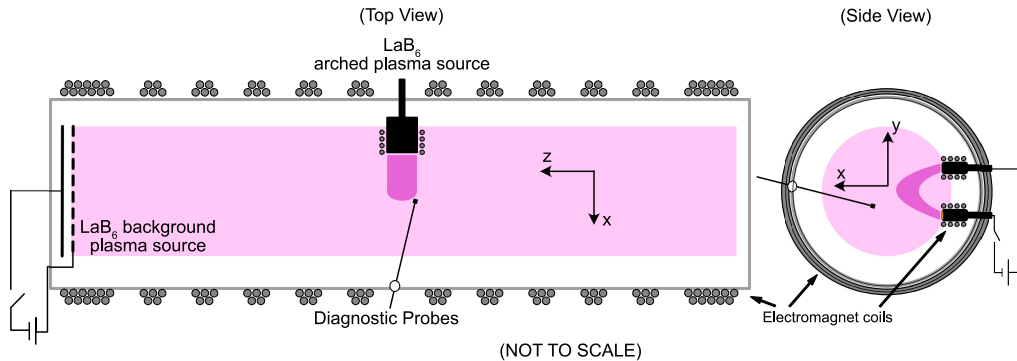


Figure 2: Schematic of the experimental setup depicting cross sections of the vacuum chamber from top (left panel) and side (right panel). The main plasma column is marked with light pink color. The arched plasma is shown in a dark-pink color in both views. These plasma sources are operated in sync using two different discharge pulsers.

configuration is identified to be a leading candidate in contemporary computer simulations (Fan 2005; Linker 2003; Gibson *et al.* 2006). The writhe and twist naturally develop in a sheared magnetic configuration, which produce sigmoidal shaped (S- or inverse-S shaped) solar filaments (Török *et al.* 2014). An association between the sign of magnetic helicity and shape of filaments (“S” or “reverse-S”) was suggested by several authors (Nakagawa *et al.* 1971). It has been observed that reverse-S shaped structures dominate on northern hemisphere of the Sun while forward-S shaped structures are more abundant on the southern hemisphere (Rust & Kumar 1996).

In this paper, dependence of the writhe of a current-carrying laboratory arched plasma on the magnitude and direction of the overlying (or ambient) magnetic field has been examined. We focus our attention on the handedness, magnitude and amount of twisting involved with respect to direction and magnitude of external magnetic field. We present our findings and offer discussion in sections below. It is worth noting that the system under investigation has plasma current well below the threshold for the kink instability ($\Phi \approx 0.3-2.5$). Therefore, observed writhe and twist of the current channel is associated with the magnetic shear produced by the combination of arched and overlying magnetic field. Emergence of axial plasma jets from the leading edge of the sheared magnetic configuration is another key observation from these experiments.

2. Experimental Setup

The experimental setup was designed with a primary goal of modeling the arched magnetized and current-carrying plasmas on the Sun. This is accomplished by driving an electrical current from two electrodes along arched vacuum magnetic field (see figures 1c and 2). The laboratory arched plasma foot-points are anchored on electrodes, while plasma itself can evolve without being perturbed by vacuum chamber walls. The experiment is performed in a cylindrical vacuum chamber (5.0 m long, 1.0 m diameter). Helium is used as background neutral gas (pressure: 5 - 9 mtorr). As shown in figure 2, external electromagnets are placed around the vacuum chamber. These electromagnets can produce up to 300 Gauss axial magnetic field inside the vacuum chamber. The axial magnetic field confines the background cylindrical plasma produced by a large LaB₆ source. It also affects the eruption dynamics of the arched plasma. The arched magnetic field is produced using two smaller electromagnets that surround the cathode and anode foot-points of the arched plasma (see the side-view in figure 2). The background plasma is

	Solar Prominence	Laboratory Arched plasma
Plasma β	$10^{-2} - 10^{-4}$	$10^{-1} - 10^{-3}$
r/r_i	$10^9 - 10^{10}$	10^2
Lundquist number	$10^{12} - 10^{14}$	$10^3 - 10^4$
Experiment time scale τ_A	150	200
Resistive diffusive time τ_A	10^{10}	>500
Aspect ratio	5	3

Table 1: Comparison of relative plasma parameters of a typical solar prominence and laboratory arched plasma.

produced by a lanthanum hexaboride (LaB₆) rectangular (20 cm x 20 cm) hot-cathode source and molybdenum wire-mesh anode separated by 30 cm. This plasma source is placed at one end of the vacuum chamber and connected to a discharge pulser (V_{\max} : 200 V, I_{\max} : 2.5 kA, Repetition rate: 0.5 Hz, pulse-width: 15 ms). The cathode is indirectly heated up to 1700°C. At this temperature the LaB₆ cathode becomes efficient in thermionic emission of electrons (Cooper & Gekelman 2013). During the discharge pulse, primary electrons from the hot cathode are accelerated, ionize the neutral gas and produce the cylindrical ambient plasma (0.6 m diameter and 4 m long, plasma density $n_e = 10^{12} \text{ cm}^{-3}$, and electron temperature $T_e = 4 \text{ eV}$). This magnetized plasma serves as a background in which the arched plasma evolves. Similar process produces an arched magnetized plasma in the middle of the device using a small hot-cathode. Two circular electrodes serving as anchors for arched plasma foot-points are mounted in the middle of the machine and connected to another discharge pulser. The arched plasma source operates in sync with the main plasma source. The cathode (7.6 cm diameter, 1800°C indirectly heated LaB₆ disk) and anode (15 cm diameter, copper disk) foot-points are shown in the bottom and top of the side-view image in figure 2. Separation between the foot-points can be varied in a range of 15 - 41 cm. Electromagnets wound around each electrode produce arched magnetic field which guides the arched plasma. A 250-450 V discharge voltage pulse (width 0.2-0.8 ms) produces a current carrying arched plasma as depicted in figure 2. Immediately after discharge and production of plasma, most of the voltage drops within thin sheaths around electrodes (size $< 0.1 \text{ mm} \ll$ arched plasma length). Therefore the dynamics of arched plasma is not significantly affected by voltage on electrodes. Typical arched plasma parameters and their comparison to solar parameters are presented in table 1. A computer-controlled 3D probe drive system and a multi-channel digitizer are used to acquire high-resolution 3D data on this experiment. Dual-tip Langmuir and three-axis magnetic loop probes are the main diagnostic probes. These probes are built using high-temperature ceramic coated wires and other components that can withstand up to 750°C temperature near the cathode foot-point of the arched plasma. This setup allows for a reliable and efficient measurement of plasma parameters (n , T_e , B) with a good spatiotemporal resolution. The experiment is highly reproducible and it operates with a high repetition rate. This facilitates measurement of the key plasma parameters in three dimensions. A fast CCD-intensifier camera (5 ns minimum exposure time, 1280 x 1024 resolution, forced air cooling, and 12 bit digital converter) is used to record the images of the plasma. Typical plasma density n_e and electron temperature T_e profiles of the arched plasma are presented in figure 3. The arched plasma current varies in the range of 50-150 A.

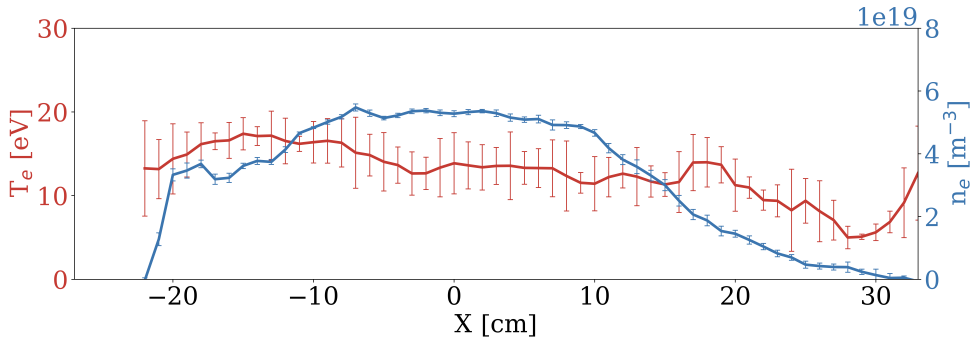


Figure 3: Profiles of electron temperature T_e (red) and plasma density n_e (blue) of the arched plasma are shown here along x axis ($y=z=0$ cm). Error bars are estimated using standard deviation in multiple measurements of n_e and T_e . The profile was acquired $800 \mu\text{s}$ after production of the arched plasma. Ambient magnetic field ($B_s = 30$ Gauss) was oriented along the z -axis.

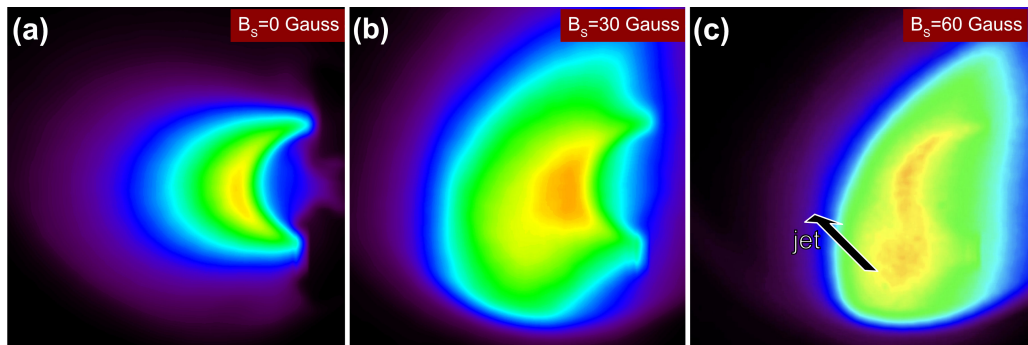


Figure 4: Unfiltered camera images of the arched plasma taken along z -axis that present the side-view perspective from figure 2. The red and yellow colors signify a higher plasma density whereas blue and purple color represent the lower density edge region of the arched plasma. Panels (a), (b), and (c) correspond to overlying background magnetic fields of 0, 30, and 60 Gauss, respectively along positive z -axis (into the page). On the last panel, plasma jet has been marked with a black arrow.

3. Results

In order to see how overlying magnetic field affects arched plasma, we conducted a series of experiments under different magnetic field configurations. Main diagnostic devices were three-axis magnetic field probe, fast camera and Langmuir probe, as described in section above. Unfiltered light camera images taken along z -axis (axis of the device) are presented in figure 4. These represent intensity of the light emitted during experiment at similar times after main trigger. The three panels in figure 4 correspond to 0, 30, and 60 Gauss background magnetic field respectively from left to right. With an increasing magnetic field strength one observes significant morphology changes, most notably the emergence of S-shape and plasma jet in panel 4c. These camera images, however, offer limited viewing perspective.

For a better understanding we turn our attention to magnetic field data obtained across volume in front of arched plasma source. Magnetic field data has been collected for three different cases of background magnetic field: 0, +30, and -30 Gauss and the results are presented in figures 5, 6,

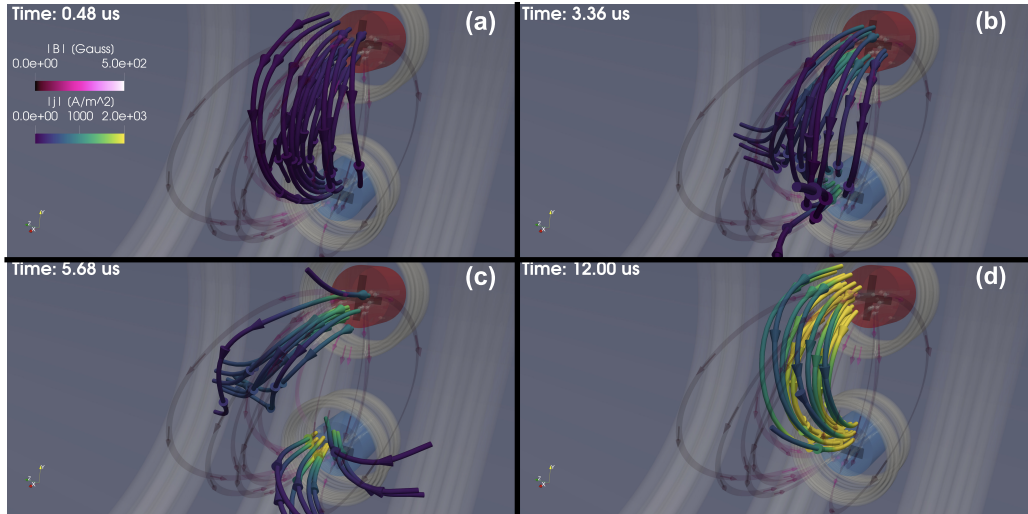


Figure 5: Visualization of data obtained using three-axis magnetic field probe at four different times after arched plasma discharge trigger: (a) $0.48 \mu\text{s}$, (b) $3.36 \mu\text{s}$, (c) $5.68 \mu\text{s}$, and (d) $12 \mu\text{s}$. The overlying magnetic field was set to 0 Gauss for all four panels. The tubular lines represent plasma current density in units of A/m^2 , while transparent ribbons represent the total magnetic field in Gauss. Color scales are placed in upper left corner. Cathode and anode are represented by blue and red cylinders with (-) and (+) signs on them respectively. Electromagnetic coils are rendered as transparent light gray tubes. The extent of current density streamlines is physically constrained by how far the probe can reach.

and 7 respectively. Raw magnetics data was processed to extract plasma current density and total magnetic field, both are represented by tubular and ribbon streamlines respectively in figures 5-7. Each panel corresponds to a different time (noted on upper left corner of each panel) after arched plasma source discharge, to give a reader sense of how plasma evolves in time. For all cases, arched plasma does not change its morphology appreciably after last panel presented in each set.

The main effect of background magnetic field on plasma is manifested by $\mathbf{J} \times \mathbf{B}$ force between plasma current and the background magnetic field. In solar case this is equivalent to large scale coronal fields (strapping fields) interacting with prominence plasma currents (Archontis *et al.* 2005; Yokoyama & Shibata 1996; Yuan *et al.* 2009). Depending on the direction of magnetic field relative to plasma current, the $\mathbf{J} \times \mathbf{B}$ force will either support or inhibit the expansion or the arched structure. More discussion on forces will follow in section below. The effect of the sign of $\mathbf{J} \times \mathbf{B}$ force on arched plasma studied here is illustrated in figure 8. The two panels in that figure show the side view (along positive z -axis) of experimental measurements of plasma current density and total magnetic field. Timing is same for both panels, with only difference being direction of overlying magnetic field: +30 and -30 Gauss for 8a and 8b respectively. In case of panel (a) the $\mathbf{J} \times \mathbf{B}$ force points inwards and leads to a higher current density close to the source. While for an opposite field, in panel (b), current is more spread out and current density in the vicinity of plasma source is considerably lower.

3.1. Discussion

Imposing overlying uniform magnetic field along the axis of the device introduced a magnetic shear to the arched guiding magnetic field. This magnetic shear in turns has a significant effect on the morphology of arched plasma under study. The camera images in figure 4 give a sense how the magnitude of background magnetic field affects the arched structure. Panel 4a corresponds

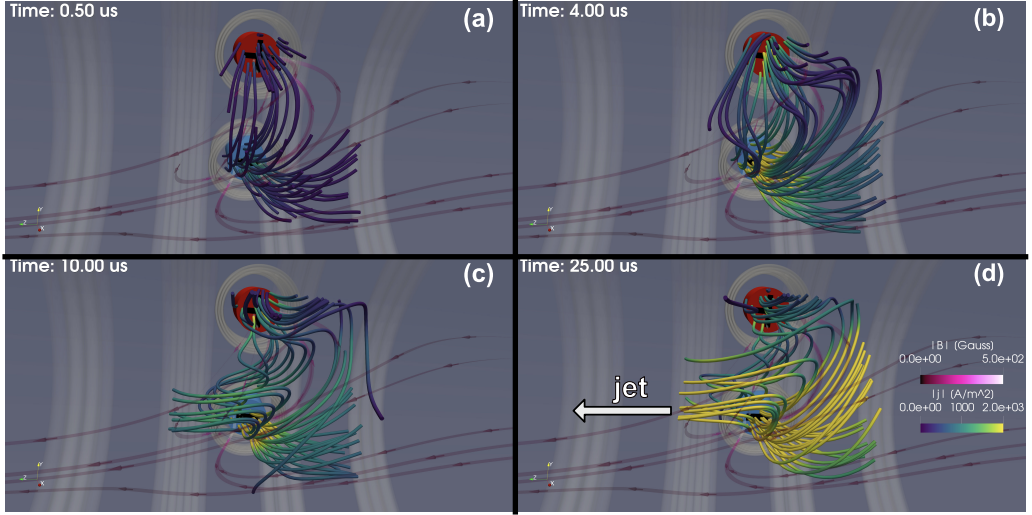


Figure 6: Visualization of data obtained using three-axis magnetic field probe at four different times after arched plasma discharge trigger: (a) $0.5 \mu\text{s}$, (b) $4 \mu\text{s}$, (c) $10 \mu\text{s}$, and (d) $25 \mu\text{s}$. The overlying magnetic field was set to 30 Gauss along positive z -axis for all four panels. The tubular lines represent plasma current density in units of A/m^2 , while transparent ribbons represent the total magnetic field in Gauss. Color scales are placed in lower right corner. Cathode and anode are represented by blue and red cylinders with (-) and (+) signs on them respectively. Electromagnetic coils are rendered as transparent light gray tubes. The extent of current density streamlines is physically constrained by how far the probe can reach. On panel (d) plasma jet has been marked with a white arrow.

to no background field, where plasma evolves to an uniform arch. Introduction of 30 Gauss axial field (figure 4b) leads to altered side profile and concentration of current density in a close vicinity of the source. This is due to an inward $\mathbf{J} \times \mathbf{B}$ force between electrical plasma current and the background field. Upon further increase of the axial magnetic field to 60 Gauss (figure 4c), one can notice the emergence of s-shape in arched plasma. Moreover, as time evolves, plasma jets develop for both 30 and 60 Gauss cases. Jets are more pronounced for stronger axial fields. This is because the location where background and arched magnetic fields connect gets closer to the arched plasma source with stronger axial magnetic field.

A more detailed picture of arched plasma morphology, its evolution in time, and dependence on different cases of axial magnetic field is offered by magnetics data. Before discussion on results from figures 5 - 8 however, it is important to note that there are three major magnetic forces acting on arched plasma. If an arch is treated as a half of torus-shaped plasma, one can distinguish three major forces acting on it in the presence of guiding and ambient magnetic fields: tension force, hoop force and strapping force. The tension force F_t is a restorative force tending to decrease the major radius of arched plasma, and it can be expressed as (Chen 1996):

$$\mathbf{F}_t = \frac{\hat{R}}{R} \int \frac{1}{\mu_0} (B_{gv}^2 - B_g^2) dS, \quad (3.1)$$

where \hat{R} is an unit vector pointing along major radius R , μ_0 is permeability of vacuum, B_{gv} is vacuum guiding magnetic field and B_g is total guiding magnetic field (includes contribution from plasma). The hoop force F_h is directed along major radius, it tends to expand arched plasma and

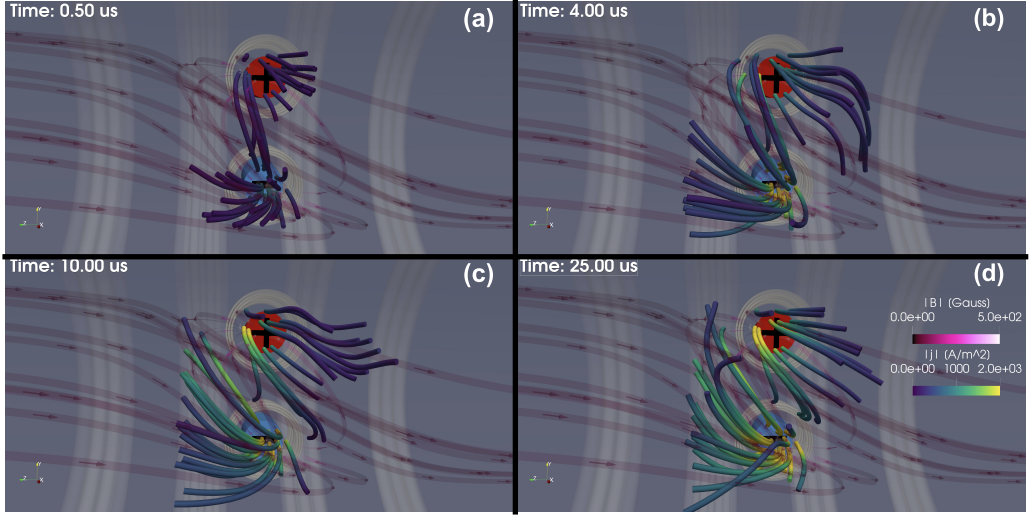


Figure 7: Visualization of data obtained using three-axis magnetic field probe at four different times after arched plasma discharge trigger: (a) $0.5 \mu\text{s}$, (b) $4 \mu\text{s}$, (c) $10 \mu\text{s}$, and (d) $25 \mu\text{s}$. The overlying magnetic field was set to 30 Gauss along negative z-axis for all four panels. The tubular lines represent plasma current density in units of A/m^2 , while transparent ribbons represent the total magnetic field in Gauss. Color scales are placed in lower right corner. Cathode and anode are represented by blue and red cylinders with (-) and (+) signs on them respectively. Electromagnetic coils are rendered as transparent light gray tubes. The extent of current density streamlines is physically constrained by how far the probe can reach.

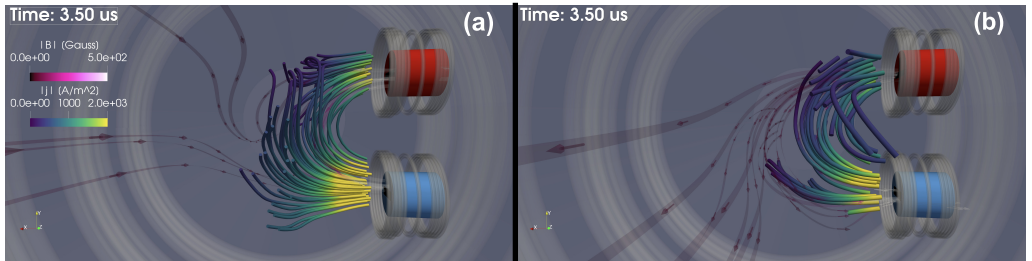


Figure 8: Visualization of data obtained with magnetic field probe for two different cases of overlying magnetic field: (a) 30 Gauss, (b) -30 Gauss along z-axis. Timing is same for both panels: $3.5 \mu\text{s}$ after discharge trigger. The tubular lines represent plasma current density in units of A/m^2 , while transparent ribbons represent the total magnetic field in Gauss. This view along z-axis offers a side view perspective. Color scales are placed in upper left corner. Cathode and anode are represented by blue and red cylinders with (-) and (+) signs on them respectively. Electromagnetic coils are rendered as transparent light gray tubes. The extent of current density streamlines is physically constrained by how far the probe can reach.

can be expressed as (Chen 1996):

$$\mathbf{F}_h = \frac{\mu_0}{2\pi R} I^2 \left[\ln \left(\frac{8R}{a} \right) - 1 + \frac{l_i}{2} \right] \hat{R}, \quad (3.2)$$

where I is the total arched plasma current, a is the minor radius, and l_i is the plasma self inductance. Finally, the strapping force F_s is essentially a $\mathbf{J} \times \mathbf{B}$ force between arched plasma

and ambient magnetic field. Depending on the direction of background magnetic field, strapping force can be either inwards (for magnetic fields along positive z-axis) or outwards (for fields along negative z-axis). For completion, force per unit length at the apex of the arched plasma is given by:

$$\mathbf{F}_s = -2IB_s\hat{R}, \quad (3.3)$$

where I is the total plasma electric current at the apex, and B_s is the magnitude of strapping field (uniform in this work).

With these forces in mind let us discuss figure 5 where the axial field was set to $B_s = 0$ Gauss. There is no strapping force and the only magnetic field present is the guiding arched magnetic field, represented by transparent ribbons. In panel 5a, at $t = 0.48 \mu\text{s}$ after discharge, arched plasma has low current density compared to following panels. As the current builds up in time (panels 5(b) and (c)), one observes shredding of current density streamlines and ejection of plasma from the arch into region outside of measurements. This phenomenon takes place on the Alfvén timescale ($\tau_A \approx 2 \mu\text{s}$). A possible mechanism for that involves a force imbalance in which the growing hoop force pushes arch outwards from the source, and leads to eruption. Arched current then recovers (figure 5d) and remains stable with no appreciable changes to its morphology for another $400 \mu\text{s}$ (until the end of discharge). Recovery of an arch is most likely a result of the system having to close the current path. In terms of twist, it is found that $\Phi = 0.3$ and the arched plasma does not show significant signs of writhe nor S-shape throughout experiment. This is expected for a total plasma current $I = 100$ A (well below kink instability threshold) and no ambient magnetic field.

Introduction of magnetic shear to this system follows by turning on uniform axial magnetic field $B_s = 30$ Gauss along positive z-axis. The total magnetic field is more complex, since now some arched magnetic field lines connect to the axial ones (see figure 6). The total plasma current in this configuration was $I = 125$ A, which is not significantly different from the case described above. In this configuration the strapping force F_s is pointing towards the source, thus inhibiting the expansion of an arched plasma. During early phase (figure 6a) arched plasma has morphology similar to that of $B_s = 0$ Gauss case (i.e.: no writhe nor twist). As current builds up, plasma tries to follow magnetic field lines. As seen in figures 6b and c, plasma starts to twist, forming a reverse S-shape. Calculations yield $\Phi \approx 2.5$. As time progresses (see panel 6d) a plasma jet forms as a result of growing current and thus hoop force pushing arched plasma away from the source towards axial field lines. This system is still well below kink instability threshold, yet plasma develops a kink-like shape, purely due to the overlying magnetic field. This is relevant to solar case where kink instability as a mechanism for solar prominence eruption is still under question. Plasma currents in solar prominences are low enough (as in this work) such that system is kink stable.

For completion and symmetry, the effects of reverse ambient field configuration where $B_s = -30$ Gauss were studied. On the sun, both directions of strapping field interacting with solar prominences were observed. For this system, the strapping force F_s points outwards, thus supporting expansion of arched plasma away from its source. The total electrical current was about $I = 75$ A. In its early stage (see figure 7a) plasma again resembles the morphology of $B_s = 0$ Gauss system. As time progresses and current builds up, plasma tries to follow sheared magnetic fields lines. This in turn leads to emergence of forward S-shaped structure as seen in figures 7c and 7d. Compared to figure 6, there is less current density streamlines connecting the electrodes. This is expected since plasma is pushed away from source by now outward strapping force. When it moves sufficiently far away from source where magnetic field lines are mostly axial, plasma escapes the arched structure. The effects of opposite strapping force are visible in figure 8. As mentioned in section 3, inward strapping force for $B_s = 30$ Gauss case (see figure 8a) leads to a larger current density near plasma source compared to $B_s = -30$ Gauss case (see

figure 8b). Since more plasma escapes the arch in case of negative ambient field, the writhe and twist are less pronounced in figure 8b. Nonetheless calculations resulted in $\Phi \approx 1.2$, which again is still below kink instability threshold.

4. Summary and Conclusions

In this work *in situ* measurements were done on laboratory arched magnetized plasma relevant to solar prominences and structures alike. It has been shown that overlying magnetic field (equivalent to strapping field in the solar case) affects the writhe, and the S-shape characteristics of the arched plasma. The electrical current of the arched plasma was well below the kink instability threshold, yet eruptive events like jets were observed. It has been found that With background magnetic fields inhibiting expansion of arched plasma, the writhe was more pronounced and plasma took reverse S-shape. In the opposite case of ambient magnetic field supporting the expansion of the arched plasma, the writhe was smaller in magnitude and plasma took forward S-shape. This suggests that the apparent writhe of a current-carrying arched plasma has a strong dependence on the structure of overlying magnetic field, not just on the magnitude of electrical current.

More comprehensive 3D data covering a broad range of overlying magnetic fields will be acquired in the future experiments to examine the role of the strength and direction of the overlying magnetic field on a kink-unstable arched plasma.

5. Acknowledgments

Authors would like to thank W. Gekelman, and S. Vincena for useful discussions and P. Pribyl, Z. Lucky, M. Drandell, and T. Ly for expert technical assistance. This research was primarily supported by funds from National Science Foundation (Award Number: PHY-1619551). The experiment is conducted at the Basic Plasma Science Facility (BaPSF) at UCLA which is supported by the DOE under Contract No. DE-FC02-07ER54918 and the NSF under Award No. PHY1561912.

REFERENCES

- ABBOT, C. 1911 *The Sun*, p. 128. New York: D. Appleton and Company.
- ARCHONTIS, V., MORENO-INSERTIS, F., GALSGAARD, K. & HOOD, A. W. 2005 The Three-dimensional Interaction between Emerging Magnetic Flux and a Large-Scale Coronal Field: Reconnection, Current Sheets, and Jets. *The Astrophysical Journal* **635** (2), 1299–1318.
- BERGER, MITCHELL A & PRIOR, CHRIS 2006 The writhe of open and closed curves. *Journal of Physics A: Mathematical and General* **39** (26), 8321.
- BURLAGA, LF 1988 Magnetic clouds and force-free fields with constant alpha. *Journal of Geophysical Research: Space Physics* **93** (A7), 7217–7224.
- CHEN, JAMES 1996 Theory of prominence eruption and propagation: Interplanetary consequences. *Journal of Geophysical Research: Space Physics* **101**, 27499–27519.
- CHEN, JAMES 2017 Physics of erupting solar flux ropes: Coronal mass ejections (cmes)-recent advances in theory and observation. *Physics of Plasmas* **24**, 090501.
- CHEN, PF 2011 Coronal mass ejections: models and their observational basis. *Living Reviews in Solar Physics* **8** (1), 1.
- COOPER, C. M. & GEKELMAN, W. 2013 Termination of a Magnetized Plasma on a Neutral Gas: The End of the Plasma. *Physical Review Letters* **110** (26), 265001.
- CREMADES, H. & BOTHMER, V. 2004 On the three-dimensional configuration of coronal mass ejections. *Astronomy & Astrophysics* **422** (1), 307–322.
- FAN, Y 2005 Coronal mass ejections as loss of confinement of kinked magnetic flux ropes. *The Astrophysical Journal* **630** (1), 543.

- FREIDBERG, JEFFREY P 1982 Ideal magnetohydrodynamic theory of magnetic fusion systems. *Reviews of Modern Physics* **54** (3), 801.
- GIBSON, SE, FAN, Y, TÖRÖK, T & KLIEM, B 2006 The evolving sigmoid: evidence for magnetic flux ropes in the corona before, during, and after cmes. *Space science reviews* **124** (1-4), 131–144.
- HILDNER, E., GOSLING, J. T., MACQUEEN, R. M., MUNRO, R. H., POLAND, A. I. & ROSS, C. L. 1975 The large coronal transient of 10 June 1973: I : Observational description. *Solar Physics* **42** (1), 163–177.
- HOOD, AW & PRIEST, ER 1981 Critical conditions for magnetic instabilities in force-free coronal loops. *Geophysical & Astrophysical Fluid Dynamics* **17** (1), 297–318.
- KRUSKAL, M & TUCK, JL 1958 The instability of a pinched fluid with a longitudinal magnetic field. *Proceedings of the Royal Society of London. Series A. Mathematical and Physical Sciences* **245** (1241), 222–237.
- LANG, K. R. 2001 *The Cambridge Encyclopedia of the Sun*, 1st edn., pp. 106–143. Cambridge, England: Cambridge University Press.
- LINKER, JON A. 2003 Models of Coronal Mass Ejections: A Review with A Look to The Future. In *AIP Conference Proceedings*, , vol. 679, pp. 703–710. Pisa (Italy): AIP, iSSN: 0094243X.
- LOW, BC 2001 Coronal mass ejections, magnetic flux ropes, and solar magnetism. *Journal of Geophysical Research: Space Physics* **106** (A11), 25141–25163.
- NAKAGAWA, Y, RAADU, MA, BILLINGS, DE & MCNAMARA, D 1971 On the topology of filaments and chromospheric fibrils near sunspots. *Solar Physics* **19** (1), 72–85.
- PRIEST, ER 1982 Solar magneto-hydrodynamics, dordrecht, holland; boston: D. *Reidel Pub. Co* pp. 79–80.
- ROSNER, R., TUCKER, W. H. & VAIANA, G. S. 1978 Dynamics of the quiescent solar corona. *The Astrophysical Journal* **220**, 643.
- RUST, DMJ 1994 Spawning and shedding helical magnetic fields in the solar atmosphere. *Geophysical Research Letters* **21** (4), 241–244.
- RUST, DAVID M & KUMAR, ASHOK 1996 Evidence for helically kinked magnetic flux ropes in solar eruptions. *The Astrophysical Journal Letters* **464** (2), L199.
- SAKURAI, TAKASHI 1976 Magnetohydrodynamic interpretation of the motion of prominences. *Publications of the Astronomical Society of Japan* **28**, 177–198.
- SHAFRANOV, VD 1957 The structure of shock waves in a plasma. *Soviet Phys. JETP* **5**.
- STURROCK, PETER A, WEBER, MARK, WHEATLAND, MICHAEL S & WOLFSON, RICHARD 2001 Metastable magnetic configurations and their significance for solar eruptive events. *The Astrophysical Journal* **548** (1), 492.
- THOMSON, A.W.P., GAUNT, C.T., CILLIERS, P., WILD, J.A., OPPERMAN, B., MCKINNELL, L.-A., KOTZE, P., NGWIRA, C.M. & LOTZ, S.I. 2010 Present day challenges in understanding the geomagnetic hazard to national power grids. *Advances in Space Research* **45** (9), 1182 – 1190.
- TÖRÖK, T & KLIEM, B 2005 Confined and ejective eruptions of kink-unstable flux ropes. *The Astrophysical Journal Letters* **630** (1), L97.
- TÖRÖK, T, KLIEM, BERNHARD, BERGER, MITCHELL A, LINTON, MARK G, DEMOULIN, PASCAL & VAN DRIEL-GESZTELYI, LIDIA 2014 The evolution of writhe in kink-unstable flux ropes and erupting filaments. *Plasma Physics and Controlled Fusion* **56** (6), 064012.
- TÖRÖK, T, KLIEM, BERNHARD & TITOV, VS 2004 Ideal kink instability of a magnetic loop equilibrium. *Astronomy & Astrophysics* **413** (3), L27–L30.
- TÖRÖK, T, PANASENCO, O, TITOV, VS, MIKIĆ, Z, REEVES, KK, VELLI, M, LINKER, JA & DE TOMA, G 2011 A model for magnetically coupled sympathetic eruptions. *The Astrophysical Journal Letters* **739** (2), L63.
- TRIPATHI, S. K. P. & GEKELMAN, W. 2010 Laboratory Simulation of Arched Magnetic Flux Rope Eruptions in the Solar Atmosphere. *Physical Review Letters* **105** (7), 075005.
- WIEGELMANN, THOMAS & SAKURAI, TAKASHI 2012 Solar Force-free Magnetic Fields. *Living Reviews in Solar Physics* **9**.
- YOKOYAMA, TAKAAKI & SHIBATA, KAZUNARI 1996 Numerical Simulation of Solar Coronal X-Ray Jets Based on the Magnetic Reconnection Model. *Publications of the Astronomical Society of Japan* **48** (2), 353–376.
- YUAN, FENG, LIN, JUN, WU, KINWAH & HO, LUIS C. 2009 A magnetohydrodynamical model for the formation of episodic jets. *Monthly Notices of the Royal Astronomical Society* **395** (4), 2183–2188.